Volume 1 | Number 1 | Jan 2013 | Pages 1–100

Soft Matter

www.rsc.org/softmatter

ROYAL SOCIETY OF CHEMISTRY

ROYAL SOCIETY OF CHEMISTRY

www.rsc.org/softmatter

ARTICLE TYPE

Nanobubble formation on a warmer substrate†

Chenglong Xu^a, Shuhua Peng^{a,b}, Greg G. Qiao^a, Voytek Gutowski^{c‡}, Detlef Lohse^d, and Xuehua Zhang^{*a,b}

The solvent exchange procedure is an often-used protocol to produce surface nanobubbles. In this procedure, the substrate is exposed to a good solvent for gas that is then mixed and rinsed with the poor solvent for gas and the nanobubbles form on the solid-liquid interface. Here we study the effects of temperatures of the substrate and the first solvent on the nanobubble formation. Atomic force microscopy with temperature control was used to examine the formation of nanobubbles at temperatures between 37°C and 54°C. It was found that the probability of nanobubble formation was larger on substrates at higher temperatures. Moreover, on warmer substrates we found nanobubbles with lateral extensions up to $8\mu m$. A morphologic analysis shows that all nanobubbles, including such giant nanobubbles, have a similar aspect ratio, independent of the substrate temperature, and that this aspect ratio corresponds to a contact angle between 13° and 22° (on the gas side), much smaller than the macroscopic counterparts. We finally discuss the implications of our results for various theories on nanobubble stability.

1 Introduction

Surface nanobubbles have attracted intensive research interest because of their peculiar properties and their potential implications to various interfacial phenomena. They may influence hydrodynamic boundary conditions, thin film stability, fine particle flotation, bimolecular adsorption and photocatalysis[1–4]. The formation of surface nanobubbles is often achieved when the solution is supersaturated with some dissolved gas, for example, by increasing the temperature, by dropping the pressure, or through (electro-)chemical reactions[5–11].

One of the most-used protocols to produce nanobubbles is the solvent exchange procedure[12,13], which essentially applies the solvent shifting technique to form nanobubbles at the solid-liquid interface. The solvent shifting technique has often been applied to the production of homogeneous nanoparticles by reducing the solute solubility in a controlled way[14–16]. Apart from the sensitivities of the solvent conditions, the solvent exchange is strongly dependant on the interfacial prop-

erties. During the solvent exchange, the substrate is firstly in contact with ethanol (a good solvent for air) which is then replaced by water (a poor solvent for air). Because air has a higher solubility in ethanol than in water, a transient gas supersaturation is locally created when ethanol is replaced by water, leading to the nucleation of surface nanobubbles. Other organic solvents, such as methanol and isopropanols can also be used in the solvent exchange[17]. Alternative to the ethanol-water exchange is the exchange of cold water with warm water[18,19], the exchange of water with salt solution[20] and the exchange of ethanol solution with salt solution[21]. Solvent exchange has also been applied to the production of interfacial liquid nanodroplets[22–24].

Although several research groups have frequently applied solvent exchange to produce nanobubbles[21,25–29], the nucleation mechanism behind the solvent exchange is still unclear and the exact conditions for the nanobubble formation remain empirical. The nanobubble nucleation is influenced by various factors, for example, the physical and chemical properties of the substrate[30], the supersaturation level of the dissolved gases[31], or the flow pattern during the mixing[32]. In particular, significant influence of the water temperature on the nanobubble nucleation has been extensively studied in previous work. Zhang *et al.* showed how the liquid temperature significantly influenced the number density of nanobubbles on mica, while the substrate was at room temperature[31].

In this work, we study how the temperatures of the substrate and the first solvent influence the formation probability and size of the nanobubbles. The range of the temperature was between 37°C and 54°C, a larger range than previously studied.

We found that the nanobubble formation probability is larger at the higher substrate temperatures, and the formed maximal nanobubble size is also larger. However, the nanobubble morphology, i.e., the typical contact angle, is unchanged, independent of the substrate temperatures and the lateral sizes of the nanobubbles.

2 Materials and Methods

2.1 Chemicals and materials

Highly ordered pyrolytic graphite (HOPG) (ZYB grade, SPI) was used as the substrate. HOPG was freshly cleaved immediately before each experiment by peeling off the outermost layers with scotch tape. The advancing contact angle of a water droplet on freshly cleaved HOPG is 81°, and the receding angle is 63°. The layered structure on HOPG from the cleavage do not change in air, water, or ethanol, so were used as the reference when we needed to relocate the same area for AFM imaging.

Water was prepared from a Milli-Q unit (Millipore Corporation, Boston, MA) and kept at 4°C for 12 hrs before it was warmed up to 37°C in a water bath before use. The dissolved oxygen level was measured by fiber optic oxygen sensor (Ocean Optics,USA). Distilled 2-propanol was used as the first solvent in the solvent exchange procedure. The liquid was handled by using syringes (Hamilton) and Teflon tubes. No one-use plastic syringes or needles were used for the liquid in the course of the experiments. All glass containers for the liquids were cleaned by 10% sodium hydroxide solution, and then rinsed by a large amount of water.

2.2 Charaterization of nanobubbles

The nanobubbles were imaged by atomic force microscopy (Multimode 8, Bruker) in the mode of PeakForce QNM (quantitative nano-mechanics). The AFM setup was equipped with a closed fluid cell and a heater between the scanner and the sample, as shown in Figure 1. Cooling water was circulated around the scanner to keep it from being overheated. With the heating accessories, our setup allows controlling the substrate temperature and imaging the surface at controlled temperature. To avoid water evaporated, we formed the nanobubbles at the preset temperature, and then reduced the system to the room temperature before the images were collected.

The cantilevers (V-shaped silicon nitride cantilevers, Veeco NP-S10) were cleaned for 15 min by UV Ozone Cleaner (Pro-Cleaner, Bioforce nanosciences) prior to the measurements. The normal spring constant of the cantilever is 0.12 N/m. The raw PeakForce QNM height images were processed using a first-order flattening after the bubbles themselves were excluded for the processing.
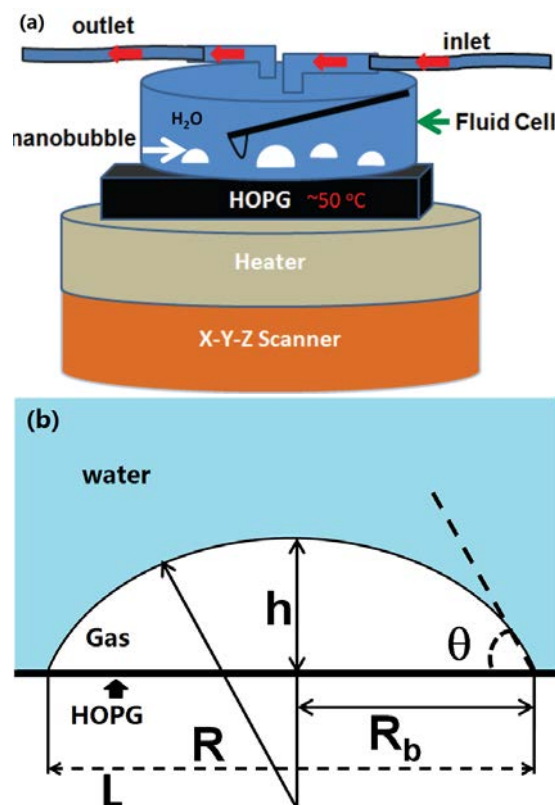

Fig. 1: (a) Schematic drawing of the experimental setup. The temperature of substrate and alcohol was kept constant at 37°C, 42°C, 51°C, and 54°C, respectively. (b) Schematic diagram of the surface nanobubbles present with typical internal contact angle θ, height h, the base radius R_b, the lateral size L and radius of the curvature R.

2.3 Formation of nanobubbles withcontrolled substrate temperature

The solvent exchange was performed inside an AFM fluid cell sealed by a silicone o-ring. Before use, the AFM fluid cell was rinsed with ethanol, a dried by stream of nitrogen and treated by UV/ozone for 15 min. The fluid cell was first mounted on the top of HOPG, and the substrate was then heated up to preset temperature. Then 2-propanol was injected into the fluid cell and the liquid inside the fluid cell quickly reached the substrate temperature. Finally, 2-propanol was exchanged very slowly by water of 37°C. Although the flow rate was not precisely controlled in the experiments, effort was taken to keep it approximately same. The total volume of water used in the exchange was approximately 20 mℓ. Care was taken to prevent any big air bubbles from sweeping over the surface during the solvent exchange process.

Table 1: Probability of bubble formation and maximal bubble size at different temperatures of HOPG substrates.

substrate temperature	formation probability	max. height (nm)	max. lateral size (nm)
37°C	5/10	108	1255
42°C	2/5	64	731
45°C	0/3	n/a	n/a
51°C	1/1	120	1295
54°C	3/4	758	8000

3　Results

The temperature of the substrate was kept at 37°C, 42°C, 45°C, 51°C, and 54°C during the solvent exchange, as listed in Table 1. At the three lower temperatures nanobubbles were produced seven out of eighteen times of the solvent exchange. In contrast, at the two higher temperatures four out of five experiments produced nanobubbles successfully. Although our numbers of experiments are limited, we can still estimate that the probability for the nanobubble formation seems to be higher on a warmer substrate.

Many of the AFM images in previous work have shown the nanobubbles produced by the solvent exchange at the temperature below 45°C. Here we focus on the new results obtained at the two higher temperatures above 50°C, for which we have the best reproducibility. The representative AFM image in Figure 2 shows the nanobubbles produced at 51°C. The cross-sectional profiles of the nanobubbles are fitted with spherical caps, from which the contact angle of nanobubbles was calculated. Figure 3 shows the image and cross-sectional profiles of bubbles produced at 54°C We found that at the temperature of 51°C or 54°C, some micrometer sized bubbles were formed concurrently with nanobubbles, and those micron-sized bubbles were visible even in optical microscopy. The distribution of the bubble size is shown in the histogram in Figure 4. Those bubbles vary from tens to hundreds of nanometers in height and hundreds nanometer to several microns in the base radius. In all imaged areas, the largest observed nanobubble is 8 μm in lateral size and 758 nm in height, as shown in Figure 3(c)(d). This is the first time that such large bubbles are produced on HOPG by the solvent exchange method.

The plots in Figure 5 show the height and lateral size of all bubbles produced at different temperature. For all of the bubbles, the height versus base radius can in first approximation be fitted with a linear relationship, implying that they would be self-similar in shape. The slope of the linear fitting for the bubbles produced at the different temperature is 0.087 at 37°C, 0.078 at 42°C, 0.087 at 51°C and 0.093 at 54°C, respectively. This slope of the straight line fit, i.e., the mean ratio h/R_b between the height h and the base radius R_b determines the mean
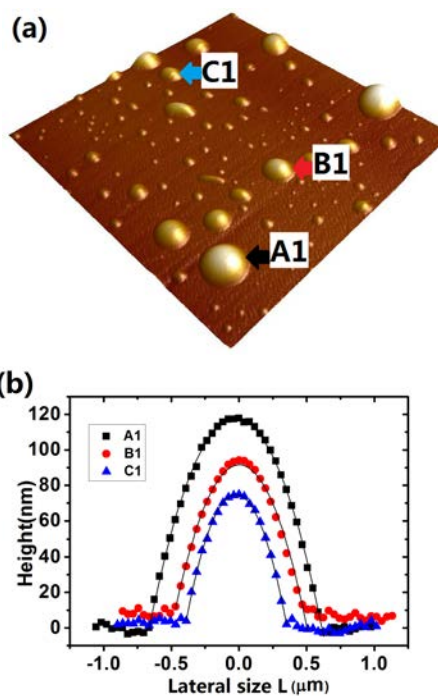
Fig. 2: Representative AFM images and crosssection of nanobubbles at 51°C. (a) AFM height image of the nanobubbles. Scan size: 10μm×10 μm. (b) Representative cross-sectional profiles of three nanobubbles in (a). The fitting radii are (A1) 1788 nm, (B1) 1415nm, and (C1) 993nm.

contact angle of the nanobubbles,

$$\tan \theta = \frac{R_b}{R-h} = \frac{2\frac{h}{R_b}}{1-\left(\frac{h}{R_b}\right)^2}. \qquad (1)$$

The mean contact angles calculated from the mean slopes in Figure 5 are 20° at 37°C, 18° at 42°C, 20° at 51°C, and 21° at 54°C, respectively. There is thus no clear correlation between the morphological features of the nanobubbles and the substrate temperature.

While from Figure 5 the overall trend and the mean contact angle can be extracted, more details are revealed when plotting the contact angle of each individual bubble itself, as done

(a)

(b)

(c)

(d)

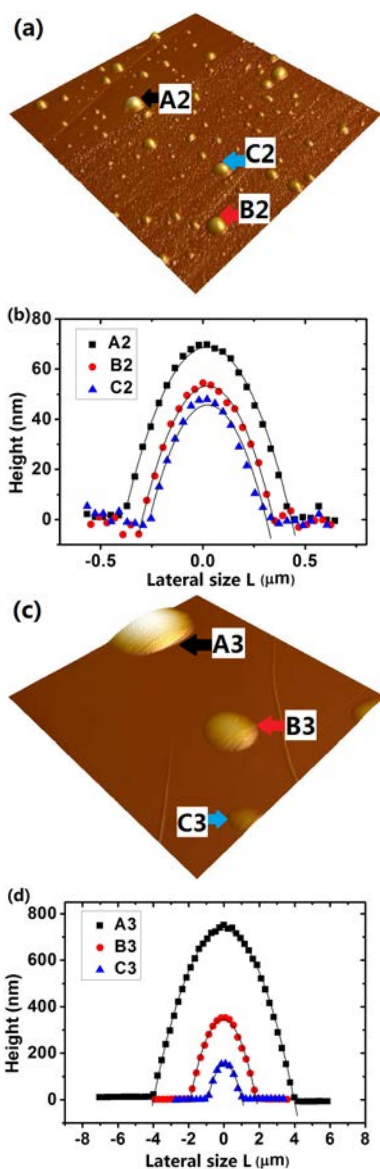Fig. 3: AFM image and representative cross-sectional profiles of nanobubbles formed at the temperature of substrate of 54°C. Scan size: (a) 10μm×10 μm, (c) 20μm×20 μm. The radii of the fitting spheres of the profiles are (A2)1257 nm, (B2) 994 nm, (C2) 917 nm, (A3) 11197 nm, (B3) 5239 nm, and (C3) 3236 nm.
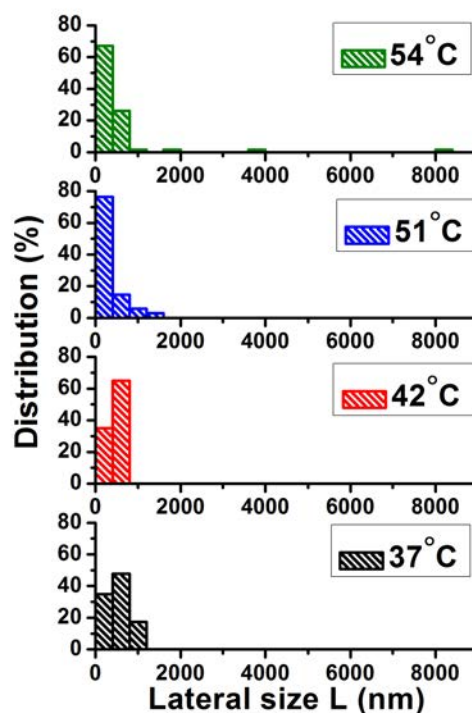

Fig. 4: Distribution of the base radius of nanobubbles produced at the temperature of 54°C, 51°C, 42°C, and 37°C.

than their macroscopic counterparts. Even a bubble with lateral size of 8μm has only a height of 760nm. Its contact angle is around 21°, much less than the ∼ 90° of the macroscopic contact angle.

For a given substrate temperature, the large variation in the formation and size of nanobubbles in the experiments can be partly due to several uncontrolled parameters and conditions. For example, the level of dissolved air in water may vary with the subtle difference in liquid handling. We measured the dissolved oxygen level in water over time and after being shaken by hand (shown in Supporting Data). Even shaking a half-filled water bottle gently by hand can already dramatically reduce the dissolved oxygen level. The nanobubble nucleation is also very sensitive to the flow mixing conditions in the experiments. We found that the geometry of the fluid cell is very important for the nanobubble formation for a given flow rate, possibly due to sensitivity of the gas saturation level to the mixing pattern during the solvent exchange.

in Figure 6. This figure reveals that the contact angle is not exactly constant but varies in a narrow range as a function of the base radius. More precisely, the contact angle of the 70 analysed individual bubbles changed from 13° to 22° as the lateral size L increases from 100nm to 8μm. This size dependence of the contact angle will be discussed extensively in the Discussion section. Here we note that all the bubbles are much flatter
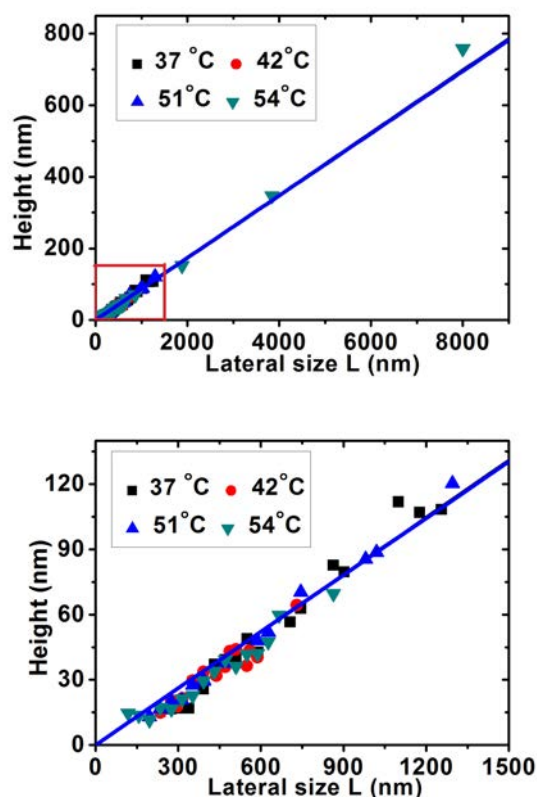
Fig. 5: Plot of the height versus lateral size of nanobubble produced at different temperatures. The data can fit with h=CL, where C is between 0.078 to 0.093. The blue line is the representative linear fitting from the data obtained on the substrate at 51°C and the fitting coefficient (R-Square) is 0.99. The lateral size of nanobubbles spans from 200nm to 8000nm. The lower panel is the blow up of the marked area in the upper panel.

4 Discussions

4.1 Temperature dependance of the formation probability

It was reported that the optimal temperature for the nanobubble nucleation was between 35°C to 40°C. In that work[33] the nanobubble formation was achieved by exposing the substrate directly to water, not by the solvent exchange process. By the same immersion process, Seddon *et al.* found that nanobubbles only formed in a certain liquid temperature range[34]. The recent theory by Petsev *et al.* also predicted that stable nanobubbles could only exist in narrow temperature ranges[35]. Here our results show that the nanobubble formation is enhanced at elevated temperatures. So the temperature dependance of nanobubble formation through the solvent exchange seems to be different from that of nanobubble formation by
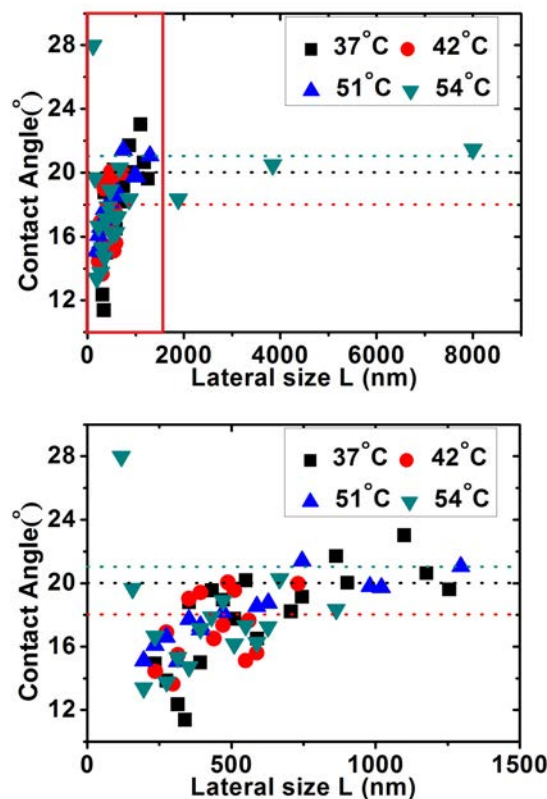

Fig. 6: Contact angle versus lateral size of nanobubbles formed at different temperature. The lower panel shows the blow up of the marked region in the upper panel. The dotted lines show the contact angles that are calculated according to Eq. 1 based on the slopes of the plots of height versus lateral size in Figure 5.

direction immersion.

The higher probability of formation and larger size of bubbles by the solvent exchange on warmer substrates may be related to the following effects: (i) A higher level of local gas supersaturation may be created when the substrate temperature is higher. The gas supersaturation originates from the solubility difference in the alcohol and water and the exothermal mixing of the two solvents. When the substrate and the alcohol were warmer than the initial temperature of water (37°C), the gas supersaturation may be further enhanced due to the decrease of gas solubility in water at higher temperature[36]. (ii) The kinetics is at elevated temperature, i.e. faster gas diffusion. For example, the diffusion coefficient of oxygen in water increases from 3.24×10^{-5} to 3.99×10^{-5} cm²/s with the temperature from 40°C to 50°C. A statistical analysis of the spatial distribution of nanobubbles and the bubble size has shown that the nucleation and growth of nanobubbles was controlled by the depletion of gas molecules out of the liquid phase[37]. As the gas molecules diffuse faster at higher temperature, a

nanobubble may take gas molecules in a larger volume of the liquid and therefore has a larger size.

Apart from temperature, the gas saturation level during the solvent exchange may be possibly influenced by other parameters, such as the actual gas saturation level in water and in alcohol, the concentration gradient of the alcohol in water during the mixing, and the heat released from the exothermic mixing. We can not disentangle the effects from all the parameters. Therefore from this work we cannot obtain the relationship between the gas solubility at different temperature and the probability of the bubble nucleation.

There are several different aspects between this work and our previous work[31]. (1) Here the probability of bubble nucleation and bubble size changed with the temperature, while previously we observed the dependance of the bubble number density on temperature; (2) the substrate in this work is hydrophobic, while the previous work was on hydrophilic mica; (3) The substrate temperature was controlled in this work, different from the control of water temperature in previous work. However, in any case the temperature is unlikely to be uniform in the entire system during the bubble nucleation, because the alcohol-water mixing is exothermic.

4.2 Length scale of nanobubbles

It has been reported that there is a length scale limitation of nanobubbles[38]. They were stable if their curvature diameters were below 2.0 μm. This was calculated from the base radius of the detached bubbles[7]. This length scale was proposed to be less than 100 nm in height from the measurements by the scanning transmission X-ray microscopy[39]. On different substrates (e.g. silanized silicon), micron-sized bubbles and nanobubbles form spontaneously by the solvent exchange at ambient conditions, possibly related to the high hydrophobicity of the substrates. Micron-sized bubbles were also inferred from the measurements between hydrophobic and hydrophilic surfaces or two hydrophobic surfaces by surface force apparatus[40,41]. Our results here showed that some microscopic bubbles formed on warmer HOPG are higher than 100 nm and larger than 2 μm in lateral diameter. So if a typical length scale of nanobubbles exists at all, it must be temperature dependent.

The giant nanobubbles (better called microbubbles) observed in this work have important implications on nanobubble stability theories. To explain the long lifetime of nanobubbles, Brenner and Lohse proposed a dynamic equilibrium theory that attributes the bubble stability to the balance between the gas out flux from the bubbles and the influx to the bubbles[42]. Later Seddon *et al.*[43] extended that theory by postulating that the gas circulation was driven by the Knudsen gas nature of the gas inside the nanobubbles. As the Knudsen gas behaviour breaks down once the height of the nanobubble is

larger than the mean free path of gas, that model naturally predicts an upper limit for the size of the nanoboubbles. However, in our experiments those bubbles with the heights of 152nm, 347nm, and 758nm shown in Figure 3 have exceeded the free pathlength of gas, which for atmospherical pressure of 1atm (the Laplace correction for these giant nanobubbles are negligible) is $\sim 147nm$ at 54°C. Those bubbles were stable for at least the period of the experiments, just as the other smaller nanobubbles. This suggests that the stability of nanobubbles is unlikely due to the Knudsen nature of the gas inside the nanobubbles. Also Liu and Zhang predict, based on a thermodynamical argument, that there is an upper limit of the nanobubble size.[44] Their theory accounts for the nanobubble stability by the surface heterogeneity.

4.3 Size dependence of the contact angle

Now we discuss the relationship between the contact angle of the nanobubbles and their base radius, see Figure 6. According to the classical Young equation[45,46], valid for macroscopic bubbles and drops, such dependence should not exist. On a nanoscale one expects deviations from Young's equation due to line tension effects, which predict a linear relation between the cosine of the contact angle and the inverse of the base radius[45–47],

$$\cos\theta = \frac{\gamma_{SL} - \gamma_{SV}}{\gamma_{LV}} - \frac{\tau}{\gamma_{LV}R_b} = \cos\theta_\infty - \frac{\tau}{\gamma_{LV}R_b}. \quad (2)$$

The first term represents the standard Young equation with γ_{SL} the solid-liquid surface energy, γ_{SV} the solid-vapor surface energy, and γ_{LV} the liquid-vapor/gas surface tension. The second term is the correction due the line tension τ. The theoretical calculations of ref.[48] and later the MD simulations of ref.[49] showed that typically $\tau \sim -(10^{-11} - 10^{-12})N$ and correspondingly $|\tau/\gamma_{LV}| \sim (0.05 - 0.5)nm$, so real line tension effects can hardly be relevant for the much larger surface nanobubbles. However, eq. (2) has been used as *effective description* for the empirically found size dependence of the contact angle, with an effective or apparent line tensions two and more orders of magnitude larger than theoretically expected, representing the effect of surface heterogeneity[50].

The cosine contact angle of nanobubbles versus the inverse of base radius is plotted in Figure 7. The data of the bubble size range from 180 nm to 8μm, which is larger than what has been considered in literature[38,47]. We notice that in the previous work the bubbles were on three different substrates[38]. Here for clarity Figure 7 only shows the data from nanobubbles on HOPG. While a larger range of bubble sizes will be highly desirable, we note that the large deviation in the contact angle may be an intrinsic property of surface nanobubbles. Increasing the data range thus may not eliminate such variations.
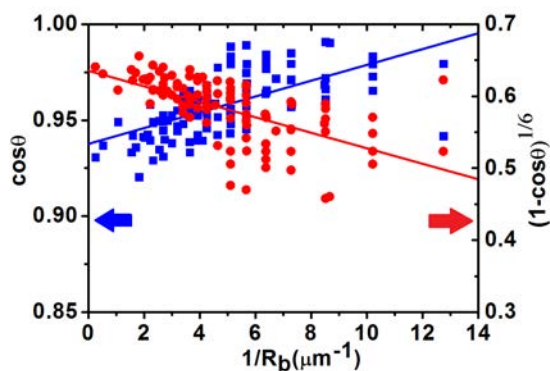
Fig. 7: Cosine of the contact angle (left axis – or function thereof – right axis) versus the inverse base radius R_b for nanobubbles formed at different temperatures. The blue line is the best fit to Eq. (2) for all the four temperatures, the red line the best fit to Eq. (3). In the chosen representations, both laws should be a straight line. The fit parameters are given in table 2.

We proceed to fit the data in Figure 7 with a linear line according to Eq. (2) and the obtained fitting parameters $r\theta_\infty$ and τ/γ_{LV} are listed in Table 2. As one can see, the effective line tension length scale $|\tau/\gamma_{LV}|$ derived from the slope of the fitting is on the order of 4 nm, which is about two orders of magnitude larger than the theoretical molecular value of the line tension [48,49]. One can also see that the microscopic infinite contact angle θ_∞ is much smaller than the macroscopically expected contact angle which one would expect based on the surface tensions.

An alternative effective description of the contact angle dependence on the length scale can be achieved within the weak heterogeneity theory. According to this theory originally described by de Gennes [45,46], droplets nucleate on the highest energy defects, then grow preferentially on the most wettable areas, possibly slightly shifting their center of mass to minimize the free energy. This tendency is balanced by the surface tension which acts as elastic restoring forces keeping the spherical cap shape of the droplets. Checco et al. [51] adopted the weak heterogeneity theory to explain the nonlinear dependance of the contact angle of nanodroplets on their base radius that was observed in their experiments. In their work, the cosine of the nanodroplet contact angle depends in a more complicated way on the inverse of the base radius R_b, namely through the relation

$$\cos\theta = 1 + \frac{S}{\gamma_{LV}}\left(1 - \frac{\delta r}{R_b}\right)^6. \qquad (3)$$

Here $S = \gamma_{SV} - \gamma_{SL} - \gamma_{LV}$ is the so-called spreading parameter and δr is an a priori unknown length scale, which can be interpreted as the difference between the nanodroplet radius and the radius of a droplet having the same volume but with the

macroscopic contact angle. It is this length scale that characterises the surface heterogeneities. In the work by Checco *et al.* it is obtained from digitising AFM images of the surface; here we consider it as pure fit parameter.

To examine whether the weak heterogeneity of the substrate might be attributed to the size dependance of the contact angles of nanobubbles, we assume that relation (3) holds for nanobubbles and fit the cosine of the contact angle according to Eq. (3). The best fitting curve is shown in Figure 7 and the two corresponding fitting parameters S/γ_{LV} and δr for each temperature are given in table 2.

As both fits Eq. (2) and Eq. (3) have two unknown parameters it is fair to compare the quality of the fits. We must say that from the precision of our data we cannot judge whether one or the other effective model to represent the surface heterogeneities is better or worse; both are consistent with the data. We stress again that τ in Eq. (2) is not the line tension but an effective or apparent line tension. More elaborate theoretic work is clearly required to better understand how the heterogeneity of the surface leads to the observed weak dependance of the nanobubble contact angle on its base radius.

Table 2: Fitting parameters for the dependance of the contact angle of nanobubbles with their base radius. θ_∞ and τ/γ_{LV} are the parameter in Eq. (2); S/γ and δr are the parameters in Eq. (3).

θ_∞	$-\tau/\gamma_{LV}$ (nm)	$-S/\gamma$	δr (nm)
20.3	4.1	0.0658	17.0

5 Conclusions

The temperature of the substrate and of the first solvent has significant effects on the nucleation probability and size of the nanobubbles produced by the solvent exchange procedure. Higher gas saturation and faster molecular diffusion at higher temperature facilitate the formation of the nanobubbles. For the higher substrate temperatures, the maximal nanobubble size can be as large as $8\mu m$. The existence of these giant nanobubbles challenges some theoretical models on nanobubble stability. The morphology of nanobubbles produced at different temperature is independent of temperature and their contact angles vary in a narrow range with the base radius. The mechanism behind the weak size dependance of the contact angle still remains unclear; we speculate that it originates from surface inhomogeneities.

Our final note is on the chemical identity of the nanobubbles observed in this work. Recent work reports that in a number of publications nanobubbles were actually due to contaminations from disposable needle or syringes [52]. In this present work,

glass syringes and Teflon tubings were used in the experiments. Liquids did not contact with any disposable syringes or needles. We recognise that so far no molecular spectroscopy has been provided to unambiguously confirm that individual nanobubbles are indeed gaseous. A simple touchstone to distinguish nanobubbles from other objects is highly desirable in the community.

Acknowledgements

References

1   P. G. de Gennes, *Langmuir*, 2002, **18**, 3413–3414.
2   M. A. Hampton and A. V. Nguyen, *Adv. Coll. Int. Sci.*, 2010, **154**, 30–55.
3   V. S. J. Craig, *Soft Matter*, 2011, **7**, 40–48.
4   L. James, R. T. Seddon Detlef, *Journal of Physics: Condensed Matter*, 2011, **23**, 133001.
5   X. H. Zhang, X. D. Zhang, J. L. Sun, Z. X. Zhang, G. Li, H. P. Fang, X. D. Xiao, X. C. Zeng and J. Hu, *Langmuir*, 2007, **23**, 1778–1783.
6   P. Attard, M. P. Moody and J. W. G. Tyrrell, *Physica a-Statistical Mechanics and Its Applications*, 2002, **314**, 696–705.
7   L. Zhang, Y. Zhang, X. Zhang, Z. Li, G. Shen, M. Ye, C. Fan, H. Fang and J. Hu, *Langmuir*, 2006, **22**, 8109–8113.
8   F. Hui, B. Li, P. He, J. Hu and Y. Fang, *Electrochem. Comm.*, 2009, **11**, 639–642.
9   Z. Wu, H. Chen, Y. Dong, H. Mao, J. Sun, S. Chen, V. S. J. Craig and J. Hu, *J. Colloid Interface Sci.*, 2008, **328**, 10–14.
10   C. Huang, J. Jiang, M. Lu, L. Sun, E. I. Meletis and Y. Hao, *Nano Lett.*, 2009, **9**, 4297–4301.
11   L. Luo and H. S. White, *Langmuir*, 2013, **29**, 11169–11175.
12   S.-T. Lou, Z.-Q. Ouyang, Y. Zhang, X.-J. Li, J. Hu, M.-Q. Li and F.-J. Yang, *J. Vac. Sci. Technol. B*, 2000, **18**, 2573–2575.
13   S. Lou, J. Gao, X. Xiao, X. Li, G. Li, Y. Zhang, M. Li, J. Sun, X. Li and J. Hu, *Materials Characterization*, 2002, **48**, 211–214.
14   J. Aubry, F. Ganachaud, J.-P. C. Addad and B. Cabane, *Langmuir*, 2009, **25**, 1970–1979.
15   K. Roger, R. Botet and B. Cabane, *Langmuir*, 2013, **29**, 5689–5700.
16   E. Aschenbrenner, K. Bley, K. Koynov, M. Makowski, M. Kappl, K. Landfester and C. K. Weiss, *Langmuir*, 2013, **29**, 8845–8855.
17   S. Yang, S. M. Dammer, N. Bremond, H. J. W. Zandvliet, E. S. Kooij and D. Lohse, *Langmuir*, 2007, **23**, 7072–7077.
18   M. Guan, W. Guo, L. Gao, Y. Tang, J. Hu and Y. Dong, *Chem. Phys. Chem*, 2012, **13**, 2115–2118.
19   X. H. Zhang, N. Maeda and V. S. J. Craig, *Langmuir*, 2006, **22**, 5025–5035.
20   W. Guo, H. Shan, M. Guan, L. Gao, M. Liu and Y. Dong, *Surf. Sci.*, 2012, **606**, 1462–1466.
21   J. Martinez and P. Stroeve, *J. Phys. Chem. B*, 2007, **111**, 14069–14072.
22   X. Zhang and W. Ducker, *Langmuir*, 2007, **23**, 12478–12480.
23   X. H. Zhang, J. M. Ren, H. J. Yang, Y. H. He, J. F. Tan and G. G. Qiao, *Soft Matter*, 2012, **8**, 4314–4317.
24   H. Yang, S. Peng, X. Hao, T. A. Smith, G. G. Qiao and X. Zhang, *Soft Matter*, 2014, 957–964.
25   S. Yang, E. S. Kooij, B. Poelsema, D. Lohse and H. J. W. Zandvliet, *EPL*, 2008, **81**, 64006.
26   M. A. Hampton, B. C. Donose and A. V. Nguyen, *J. Colloid Interface Sci.*, 2008, **325**, 267–274.
27   L. A. Palmer, D. Cookson and R. N. Lamb, *Langmuir*, 2011, **27**, 144–147.
28   N. Ishida, Y. Kusaka and H. Ushijima, *Langmuir*, 2012, **28**, 13952–13959.
29   V. Belova, M. Krasowska, D. Wang, J. Ralston, D. G. Shchukin and H. Moehwald, *Chem. Sci.*, 2013, **4**, 248–256.
30   X. Zhang and N. Maeda, *J. Phys. Chem. C*, 2011, **115**, 736–743.
31   X. H. Zhang, X. D. Zhang, S. T. Lou, Z. X. Zhang, J. L. Sun and J. Hu, *Langmuir*, 2004, **20**, 3813–3815.
32   X. H. Zhang, A. Quinn and W. A. Ducker, *Langmuir*, 2008, **24**, 4756–4764.
33   M. A. J. van Limbeek and J. R. T. Seddon, *Langmuir*, 2011, **27**, 8694–8699.
34   J. R. T. Seddon, E. S. Kooij, B. Poelsema, H. J. W. Zandvliet and D. Lohse, *Phys. Rev. Lett.*, 2011, **106**, 056101.
35   N. D. Petsev, M. S. Shell and L. G. Leal, *Phys. Rev. E*, 2013, **88**, 010402(R).
36   R. Battino, T. R. Rettich and T. Tominaga, *Journal of Physical and Chemical Reference Data*, 1984, **13**, 563–600.
37   H. Lhuissier, D. Lohse and X. Zhang, *Soft Matter*, 2014, **10**, 942–946.
38   L. Zhang, X. Zhang, Y. Zhang, J. Hu and H. Fang, *Soft Matter*, 2010, **6**, 4515–4519.
39   L. Zhang, B. Zhang, L. Zhao, Z. Xue, Y. Guo, H. Dong, R. Fang, J. Tai and Hu, *Journal of synchrotron radiation*, 2013, **20**, 413–418.
40   A. Faghihnejad and H. Zeng, *Langmuir*, 2013, **29**, 12443–12451.
41   A. Faghihnejad and H. Zeng, *Soft Matter*, 2012, **8**, 2746–2759.
42   M. P. Brenner and D. Lohse, *Phys. Rev. Lett.*, 2008, **101**, 214505.
43   J. R. T. Seddon and D. Lohse, *J. Phys.: Condens. Matter*, 2011, **23**, 133001.
44   Y. Liu and X. Zhang, *J. Chem. Phys.*, 2013, **138**, 014706.
45   P. G. de Gennes, *Rev. Mod. Phys.*, 1985, **57**, 827–863.
46   P. G. de Gennes, F. Brochard-Wyart and D. Quere, *Capillarity and wetting phenomena: drops, bubbles, pearls, waves*, Springer, 2004.
47   J. Yang, J. Duan, D. Fornasiero and J. Ralston, *J. Phys. Chem. B*, 2003, **107**, 6139–6147.
48   T. Getta and S. Dietrich, *Phys. Rev. E*, 1998, **57**, 655–671.
49   J. H. Weijs, A. Marchand, B. Andreotti, D. Lohse and J. H. Snoeijer, *Phys. Fluids*, 2011, **23**, 022001.
50   J. Joanny and P. de Gennes, *J. Chem. Phys.*, 1984, **81**, 552.
51   A. Checco, P. Guenoun and J. Daillant, *Phys. Rev. Lett.*, 2003, **91**, 186101.
52   R. P. Berkelaar, E. Dietrich, G. A. M. Kip, E. S. Kooij, H. J. W. Zandvliet and D. Lohse, *Soft Matter*, 2014, **10**, 4947–4955.